




Publication Year	2021
Acceptance in OA @INAF	2022-01-05T10:05:47Z
Title	The extension of the Fundamental Metallicity Relation beyond the BPT star-forming sequence: evidence for both gas accretion and starvation
Authors	Kumari, Nimisha; Maiolino, Roberto; Trussler, James; MANNUCCI, FILIPPO; CRESCI, GIOVANNI; et al.
DOI	10.1051/0004-6361/202140757
Handle	http://hdl.handle.net/20.500.12386/31313
Journal	ASTRONOMY & ASTROPHYSICS
Number	656

The extension of the fundamental metallicity relation beyond the BPT star-forming sequence: Evidence for both gas accretion and starvation

Nimisha Kumari^{1,2,3} , Roberto Maiolino^{2,3}, James Trussler^{2,3}, Filippo Mannucci⁴, Giovanni Cresci⁴, Mirko Curti^{2,3}, Alessandro Marconi^{5,4}, and Francesco Belfiore⁴

¹ AURA for the European Space Agency, Space Telescope Science Institute, 3700 San Martin Drive, Baltimore, MD 21218, USA
e-mail: kumari@stsci.edu

² Kavli Institute for Cosmology, University of Cambridge, Cambridge CB3 0HA, UK

³ Cavendish Laboratory, University of Cambridge, Cambridge CB3 0HE, UK

⁴ INAF – Osservatorio Astrofisico di Arcetri, Largo E. Fermi 5, 50125 Firenze, Italy

⁵ Dipartimento di Fisica e Astronomia, Università di Firenze, via G. Sansone 1, Sesto F.no (FI), Italy

Received 8 March 2021 / Accepted 20 August 2021

ABSTRACT

Context. The fundamental metallicity relation (FMR) of galaxies is a 3D relation between the gas-phase metallicity, stellar mass, and star-formation rate (SFR). So far, it has only been studied for galaxies identified as star forming (SF) on the BPT diagrams (BPT-SF), but not for galaxies with LI(N)ER/AGN classification (BPT-non-SF), mainly because of the lack of diagnostics for estimating their gas-phase metallicities in the latter cases.

Aims. We extend the FMR to BPT-non-SF galaxies.

Methods. To this end, we exploit the recent nebular line empirical calibrations derived specifically for galaxies classified as non-SF in the BPT diagrams. Moreover, we study an alternative representation of the FMR where we consider the offsets in metallicity and SFR with respect to main sequence (MS) galaxies.

Results. We find that galaxies with SFR higher than the MS are more metal-poor than their counterparts on the MS, which is interpreted in terms of gas accretion boosting star formation and diluting the metallicity. Low-mass galaxies below the MS (i.e. towards quiescence) have higher metallicities than their MS counterparts, which is interpreted in terms of starvation (i.e. suppression of fresh gas supply) hampering star formation and reducing the dilution effect, hence resulting in a higher level of internal chemical enrichment. Massive galaxies below the MS have a gas metallicity that is much closer to their MS counterparts and much lower than expected from their stellar metallicities; this result suggests a scenario where massive nearly quiescent galaxies with LI(N)ER-like nebular emission have recently accreted gas from the circum/intergalactic medium.

Key words. ISM: abundances – evolution – galaxies: evolution – galaxies: abundances

1. Introduction

The metallicity scaling relations of galaxies provide important information on galaxy evolutionary processes and tight constraints to models and numerical cosmological simulations (Maiolino & Mannucci 2019). The tightest scaling relation is between the stellar mass of galaxies and their gas-phase metallicity, the so-called mass–metallicity relation (MZR, Lequeux et al. 1979; also see Tremonti et al. 2004), which is often interpreted in terms of the deeper gravitational potential well of massive galaxies being more effective in retaining metals than low-mass galaxies. However, additional secondary relations of the gas metallicity with other galactic properties have been found. Mannucci et al. (2010) utilised the vast dataset of star-forming (SF) emission line galaxies from the seventh data release (Abazajian et al. 2009) of the Sloan Digital Sky Survey (SDSS, York et al. 2000) to explore the relationship between the galactic stellar mass (M_*), star-formation rate (SFR), and gas-phase metallicity ($12 + \log(\text{O}/\text{H})$). Following the works of Ellison et al. (2008), Mannucci et al. identified a secondary relation according to which, at a given stellar mass, the gas-phase metallicity of galaxies is anticorrelated with the SFR. This anticorrelation has

been interpreted in terms of gas accretion from the intergalactic and circumgalactic medium which dilutes the gas metallicity and fosters star formation. Mannucci et al. (2010) showed that the resulting three-dimensional (3D) relation between stellar mass, SFR, and metallicity exhibits little scatter in metallicity. This 3D relation was also found not to evolve in redshift, and was dubbed the fundamental metallicity relation (FMR).

Several studies based on observations (e.g., Mannucci et al. 2011; Cresci et al. 2012, 2019; Brisbin & Harwit 2012; Yates et al. 2012; Roseboom et al. 2012; Andrews & Martini 2013; Nakajima & Ouchi 2014; Salim et al. 2014; Lian et al. 2015; Hunt et al. 2016; Kashino et al. 2016; Telford et al. 2016; Curti et al. 2020), simulations (e.g., Davé et al. 2011; De Rossi et al. 2015, 2017; Lagos et al. 2016; Genel 2016; Matthee & Schaye 2018; Torrey et al. 2018; Bustamante et al. 2018), and analytical models (e.g., Dayal et al. 2013; Lilly et al. 2013; Forbes et al. 2014; Spitoni et al. 2017) have explored various aspects of the FMR. Though most observational studies agree on the general shape of the FMR, there has been disagreement over the FMR behaviour typically at high stellar masses, which is thought to depend on various systematic effects such as selection of galaxies on the basis of signal-to-noise ratio (S/N)

in emission lines (e.g., Yates et al. 2012; Telford et al. 2016) and calibration methods of SFR and gas-phase metallicities (e.g., Andrews & Martini 2013; Cresci et al. 2019). The overall normalisation of the FMR is shown to depend critically on the adopted metallicity calibration (Curti et al. 2020). The physics of the FMR is well explained by analytical models (e.g., Dayal et al. 2013; Lilly et al. 2013) whereby different components of the gas-regulator model play significant roles in shaping its form.

Some studies (e.g., Bothwell et al. 2013, 2016a; Brown et al. 2018) have explored a similar relation where the SFR is replaced by the gas content, finding that, once the much lower statistics is taken into account, the resulting 3D relation is even tighter. More specifically, the anticorrelation between metallicity and gas content is tighter than the anticorrelation between metallicity and SFR, suggesting that the former is more fundamental while the latter is a byproduct resulting from the dependence of the SFR on gas via the Schmidt-Kennicutt relation (Schmidt 1959; Kennicutt 1998). These findings further support the interpretation that the primary driver of the FMR is gas accretion diluting the gas-phase metallicity and fostering star formation.

The existence of the FMR has also been explored on spatially resolved scales (e.g., Barrera-Ballesteros et al. 2017; Cresci et al. 2019; Sánchez Almeida & Sánchez-Menguiano 2019; Sánchez et al. 2019) using the integral field spectroscopic data from surveys such as MaNGA (Bundy et al. 2015), CALIFA (Sánchez et al. 2012), and SAMI (Bryant et al. 2015). Although different studies have reached somewhat different conclusions, there are indications that the FMR also holds for subgalactic regions (see discussion in Maiolino & Mannucci 2019). Questions have also been raised about the evolution of the FMR with redshift (e.g., Mannucci et al. 2010; Troncoso et al. 2014; Sanders et al. 2018, 2020; Cresci et al. 2019). It has been shown that once the metallicity calibrations and uncertainties are taken into account, the FMR does not evolve up to $z \sim 2.5$ and possibly even to $z \sim 3.5\text{--}4$ (Cresci et al. 2019; Sanders et al. 2020), although testing the evolution to very high redshift is made difficult by the potential evolution of the metallicity diagnostics and the limited availability of metallicity tracers with ground-based observations.

The existence of the FMR has also been used to explain the redshift evolution of the mass–metallicity relation (Maiolino et al. 2008; Troncoso et al. 2014; Mannucci et al. 2010; Sanders et al. 2020), in the sense that high-redshift galaxies show more active star formation and therefore populate the region of the FMR with lower metallicities, resulting in evolution of the MZR.

However, past observational studies of the FMR have only focused on those galaxies classified as star forming according to the classical emission line diagnostic diagrams (the so-called BPT diagrams Baldwin et al. 1981; Kewley et al. 2006; Kauffmann et al. 2003a). This is primarily because the nebular line metallicity diagnostics (derived either empirically or through photoionisation models) have mostly been calibrated on, and therefore applicable to, ‘star forming’ galaxies classified as such based on the BPT diagrams. These diagrams provide a useful way to broadly divide the excitation mechanism of the interstellar medium in galaxies in different classes, specifically galaxies that have ongoing star formation and host young O and B stars, and the population of non star-forming galaxies such as those with a low-ionisation (sometimes nuclear) emission region (LI(N)ERs, Belfiore et al. 2016), with little star formation activity and possibly ionised by evolved asymptotic giant branch (AGB) stars, post-AGB stars (Singh et al. 2013),

white dwarfs (Stasińska et al. 2008), shocks (Heckman 1980), or radiation leaked by star forming regions, as well as active galactic nuclei (AGNs) powered by a central mass-accreting super-massive black hole. However, different types of galaxies are classified in these diagrams by ‘razor-cut’ dividing lines, which are certainly over-simplistic demarcations. The distribution of galaxies in these diagrams is not bimodal, but shows a continuous distribution across the dividing lines. It is unrealistic to think that galaxies suddenly change excitation mechanism as they cross the dividing lines. Variation in properties such as nitrogen abundance, ionisation parameter, and age of the stellar population can result in galaxies spreading beyond the dividing lines without necessarily implying a change in excitation mechanism. Therefore, imposing a sharp selection based on an assumed dividing line in the BPT diagrams may introduce biases in the galactic properties and therefore in the inferred scaling relations with metallicity. Moreover, the nebular lines used in the BPT diagrams are also used in most metallicity diagnostics; therefore selecting galaxies through line ratios that are somehow linked with the ratios used to measure the metallicity may result in biases in the resulting metallicity measurements. Ideally, the selection of galaxies should not rely on any selection based on nebular line ratios that are used to measure the metallicity of galaxies or can bias the properties of the selected galaxy population.

An additional problem in selecting only star forming galaxies based on their BPT classification is that it limits our capability of fully exploring the metallicity scaling relations even beyond ‘classical’ star forming galaxies on the BPT diagram. When galaxies decrease their star formation and move towards quiescence, they generally still have large amounts of gas (Gobat et al. 2018), but this remaining gas no longer has the emission line ratios of that found in star forming galaxies. When detected in nebular emission lines, quiescent or ‘green valley’ galaxies generally have LI(N)ER-like emission line ratios (Belfiore et al. 2018), which are typically associated with diffuse ionized gas (DIG) excited either by evolved stars (e.g., hot post-AGB stars), or by hardened, leaked radiation from residual star forming regions, as discussed above. However, as the metallicity diagnostics for galaxies in this region of the BPT diagram have not been calibrated until recently, these important stages of galaxy evolution have not been included in the metallicity scaling relations. Chemical evolution studies of non star-forming galaxies have been restricted to the use of stellar metallicities (Gallazzi et al. 2014; Peng et al. 2015; Spitoni et al. 2017; Trussler et al. 2020, 2021), analytical models (Spitoni et al. 2017), and cosmological simulations (Romeo Velonà et al. 2013) where gas-phase metallicity measurements are not needed. It is important to investigate the same process by probing the gas phase metallicities in green valley and passive galaxies.

The main hinderance to addressing the various issues outlined above, that is, extending the FMR to galaxies classified as non star-forming in the BPT diagrams, has been the lack of suitable metallicity calibrators for estimating the gas-phase metallicity of such systems. In order to overcome this problem, Kumari et al. (2019) utilised the IFS data of 24 nearby star-forming galaxies taken with the MUSE instrument on the Very Large Telescope (VLT) to identify and correct biases in the metallicity measurements of low-ionisation emission regions (LIERs), or regions dominated by DIG. The method used by these latter authors consists in comparing the emission line properties of LIER and DIG regions to those of nearby H II regions with similar levels of chemical enrichment, thus devising novel

calibrations for the DIG and LIERs. As the emission line ratios of DIG and LIERs fall on the same region occupied by the galaxy populations classified as non star-forming in the BPT diagrams, the DIG and LIER calibrators are also applicable to the non star-forming, passive, and quiescent galaxy populations, and hence enable measurements of their gas-phase metallicities (see discussion in Kumari et al. 2019).

The aim of this paper is to extend the FMR to the massive emission line galaxies lying beyond the star-forming sequence on the BPT diagrams. Henceforth, we use the terms ‘BPT-SF’ for galaxies lying below the dividing star-forming line on the classical BPT diagrams (Fig. 1), while ‘BPT-non-SF’ refers to galaxies lying beyond the dividing star forming line on the BPT diagram and occupied by AGNs and LI(N)ERs, as explained in more detail in Sect. 2. We mainly focus on emission line galaxies because the gas-phase metallicities of these systems can be estimated from the recent prescriptions from Kumari et al. (2019) based on the strong emission lines $H\beta$, $[O III]\lambda 5007$, $H\alpha$, and $[N II]\lambda 6584$. For this purpose, we use the vast dataset of SDSS-DR7 available from the Max Planck for Astrophysics and Johns Hopkins University groups (MPA-JHU) which has successfully been used for such studies in the past. We not only study the conventional form of FMR (i.e. the 3D relation between M_* , SFR, and $12 + \log(O/H)$), but we also build upon the previous work of Peng et al. (2015) and Trussler et al. (2020) to explore the difference in gas-phase metallicity between green valley+quiescent galaxies and the main sequence (MS) galaxies, while considering the offset in their SFR activity from the MS population, in order to investigate their chemical composition and processes that might lead to quenching.

The paper is organised as follows. Section 2 describes the SDSS dataset and the selection criteria, along with the methods to estimate the gas-phase and stellar metallicities, stellar masses and star-formation rates of BPT-SF and BPT-non-SF galaxies in the sample. Section 3 presents the FMR for the BPT-SF sample, the BPT-non-SF sample, and the combined sample of BPT-SFs and BPT-non-SFs, where we use the $[N II]$ -BPT and $[S II]$ -BPT diagnostic diagrams to classify the SF and non-SF galaxies. We also study an alternative representation of the FMR for the combined sample of BPT-SF and BPT-non-SF galaxies for an easier interpretation. In Sect. 4 we discuss and summarise our main results.

2. Sample selection and measurement of FMR parameters

2.1. Galaxy sample

We use the SDSS-DR7 MPA-JHU catalogue¹, which provides emission line fluxes, star-formation rates, and stellar masses. As we describe in Sect. 2.2, our analysis is dependent on the use of the $[N II]$ -BPT diagnostic diagram for applying the metallicity calibrations, as this is the diagram used by Curti et al. (2017) to select SF galaxies for their empirical calibration, which has been extended by Kumari et al. (2019) to the non-SF regions. However, we note that the results do not change significantly if the classification of galaxies (used to apply the metallicity calibrations) is based on the $[S II]$ -BPT diagram (the results based on this classification are shown in Appendix A). We apply an S/N cut of 3 on the $H\alpha$ and $H\beta$ lines and an S/N cut of 2 on $[O III]\lambda 5007$ and on $[N II]\lambda 6584$. Such an S/N cut

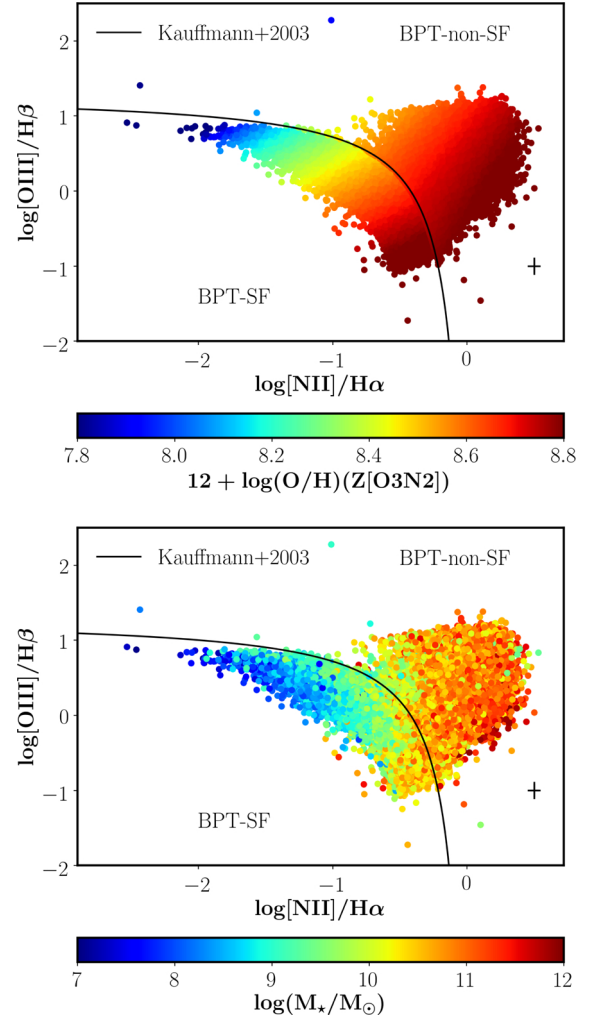


Fig. 1. $[O III]/H\beta$ versus $[N II]/H\alpha$ diagram. In the *upper panel*, the data points are colour coded with respect to the gas-phase metallicity ($12 + \log(O/H)$) using the O3N2 diagnostic. We use recipes given in Curti et al. (2017) and Kumari et al. (2019) to estimate gas-phase metallicities of BPT-SF and BPT-non-SF galaxies, respectively. In the *lower panel*, the data points are colour coded with respect to stellar mass. In both panels, the solid black curve corresponds to the line dividing star forming galaxies from non star-forming galaxies empirically derived by Kauffmann et al. (2003a), where the galaxies lying below and beyond solid black curves are referred to as BPT-SF and BPT-non-SF galaxies, respectively. The error bars in the bottom-right corner show the uncertainty on the emission line ratios.

ensures clean BPT diagnostic diagrams with no spurious line ratios. We verified that the results do not change significantly by increasing the S/N thresholds; this simply results in lower statistics. In addition to S/N cuts, we also remove all galaxies whose photometric flags consist of DEBLEND_NOPEAK or DEBLEND_AT_EDGE, and restrict the sample to galaxies with total stellar masses in the range of 10^7 – $10^{13} M_{\odot}$ thus ensuring the inclusion of low-mass dwarfs as well as massive galaxies. Different studies have assumed different redshift cuts in previous FMR studies. We find that a lower limit on redshift does not affect the higher-mass end of the FMR, which is the regime we want to probe in this work. Nevertheless, we have imposed a redshift cut of $z > 0.016$, which ensures that the SDSS fibres cover at least ~ 1 kpc on the selected galaxies. This results in a sample of $\sim 10^5$ galaxies.

¹ Available at <http://www.mpa-garching.mpg.de/SDSS/DR7>

2.2. Gas-phase metallicity

We aim to extend the FMR study to the BPT-non-SF galaxies which requires their metallicity calibration. As already discussed, Kumari et al. (2019) provides the first metallicity calibrations for the DIG/LIER and BPT-non-SF galaxies. These empirical calibrations for BPT-non-SF galaxies are based on two distinct diagnostics, O3N2 ($=\log([\text{O III}]/\text{H}\beta) - \log([\text{N II}]/\text{H}\alpha)$) and O3S2 ($=\log([\text{O III}]/\text{H}\beta) + [\text{S II}]/\text{H}\alpha$). However, the O3S2 values exhibited by the full SDSS sample selected here lie within ~ -0.4 – 1.6 , which is beyond the range in which the O3S2 diagnostic has been calibrated (~ -0.5 – 0.8 , see e.g., Maiolino & Mannucci 2019). Hence, we only use metallicities derived from the O3N2 diagnostic for the entire analysis.

Figure 1 (upper-panel) shows the [N II]-BPT diagnostic diagram (i.e. $[\text{O III}]/\text{H}\beta$ versus $[\text{N II}]/\text{H}\alpha$) along with the empirical starburst line from Kauffmann et al. (2003a), which is used to classify the SF and non-SF galaxies. We do not remove the AGNs from non-SF sample as such a recipe is not available for the [N II]-BPT diagram. Moreover, Kumari et al. (2019) make the case that their new metallicity calibration also extends to the AGN/Sy population (thanks to the $[\text{O III}]/\text{H}\beta$ corrective term mentioned below), though further tests on AGNs are required. Nevertheless, in Appendix A we show that the inclusion or removal of AGNs (based on the [S II]-BPT classification) hardly affects the overall results.

In Fig. 1 (upper-panel), BPT-SF and BPT-non-SF samples are colour coded with respect to their gas-phase metallicities, which are estimated using the empirical prescriptions given in Curti et al. (2017) and Kumari et al. (2019), and can also be expressed as the following equations.

$$12 + \log(\text{O}/\text{H})_{\text{BPT-SF}} = 7.64 + 0.22 \times \sqrt{25.25 - 9.072 \times \text{O3N2}}, \quad (1)$$

$$12 + \log(\text{O}/\text{H})_{\text{BPT-non-SF}} = 7.673 + 0.22 \times \sqrt{25.25 - 9.072 \times \text{O3N2}} + 0.127 \times \text{O3}, \quad (2)$$

where $\text{O3} = \log([\text{O III}]/\text{H}\beta)$.

2.3. Stellar metallicity

We use the gas-phase metallicities of BPT-SF and BPT-non-SF galaxies for the majority of our analysis. However, we also compare these results with stellar metallicities of the sample of MS, green valley, and passive galaxies taken from Trussler et al. (2020). Briefly, a χ^2 -minimisation code FIREFLY (Wilkinson et al. 2017) is used to fit the input galaxy spectra using a combination of stellar population models of Maraston & Strömbäck (2011), stellar spectra from the MILES (Sánchez-Blázquez et al. 2006), and stellar libraries assuming a Kroupa initial mass function (Kroupa 2001), from which mass-weighted stellar metallicities are obtained.

2.4. Stellar mass

We use the total stellar masses of our galaxy sample from the MPA-JHU catalogue. These are obtained using fits to the total photometric magnitudes of these galaxies and are different from the method based on spectral indices adopted by Kauffmann et al. (2003b) or Gallazzi et al. (2005), though these differences are quite small (a median offset of -0.01 dex between mass estimates from spectral indices and photometric magni-

tudes²). We have restricted our sample to a stellar mass range of $10^{7-13} M_{\odot}$.

The lower panel of Fig. 1 shows the distribution of galaxies in our sample on the [NII]-BPT diagram, colour coded according to stellar mass. The figure clearly shows that studies selecting only BPT-SF galaxies miss a large population of massive galaxies.

2.5. Star-formation rate

We obtain the SFR of all galaxies including the SF galaxies, LINERs, AGNs, and composite galaxies from the MPA-JHU catalogue. These SFR estimates are obtained by fitting the models of Charlot & Longhetti (2001) to the SF galaxies as discussed in Brinchmann et al. (2004) with slight modifications³, for LINERs, AGNs, composite, and low S/N SF galaxies. Some of these modifications correspond to estimating the average conversion factor from observed $\text{H}\alpha$ luminosity to SFR for low-S/N galaxies, different dust-attenuations, and appropriate aperture corrections for galaxies with low levels of star-formation following Salim et al. (2007).

We use the SFR estimates from the MPA-JHU catalogue mainly because it provides the SFR within the 3 arcsec aperture of the SDSS fibre. The other SFR estimates of the SDSS sample (e.g., Salim et al. 2016; Bourne et al. 2016; Oemler et al. 2017) may provide an improvement over the total SFR estimates from the MPA-JHU catalogue but are not suitable for the purposes of this work. As the eventual aim of our work is to study the correlation between SFR and gas-phase metallicity, it is more appropriate to study these quantities within the same spatial region. In particular, gas accretion resulting in metallicity dilution and a boost in star formation can only be properly probed by measuring metallicity and SFR in the same aperture. Given that we only have information on the gas-phase metallicity within the galactic region covered by the fibre, we prefer to use the fibre SFR. Stellar mass, on the other hand, acts more like a clock, telling us about the evolutionary stage of a galaxy (see Sect. 4) and also trace the overall gravitational potential well of the galaxy; we therefore use the total M_{\star} in this work.

We note that a few FMR studies (e.g., Mannucci et al. 2010) have estimated SFRs from $\text{H}\alpha$ luminosities following the prescription of Kennicutt (1998). However, this calibration is only suitable for SF galaxies or H II regions as there is an inherent assumption of photoionisation by hot O and B stars, rather than other more evolved stellar populations (or even AGNs) which are likely the source of ionisation within non-SF galaxies.

Figure 2 shows SFR versus M_{\star} for the BPT-SF (upper-panel) and BPT-non-SF (lower-panel) samples identified on the basis of the [N II]-BPT selection. The location of the star formation MS shown in this figure is derived by taking the median of the SFRs of the BPT-SF galaxies in the stellar mass bins of 0.3 dex. We note that different definitions of the MS have been proposed by various groups, (e.g., Renzini & Peng 2015; Popesso et al. 2019) which are valid in different stellar mass ranges and generally fitted by a linear form, but may show bending depending on the SFR recipes adopted. However, these other studies use the total SFR and stellar mass, and their results are therefore not suitable for this work which uses the star-formation activity within the

² https://wwwmpa.mpa-garching.mpg.de/SDSS/DR7/mass_comp.html

³ <https://wwwmpa.mpa-garching.mpg.de/SDSS/DR7/sfrs.html>

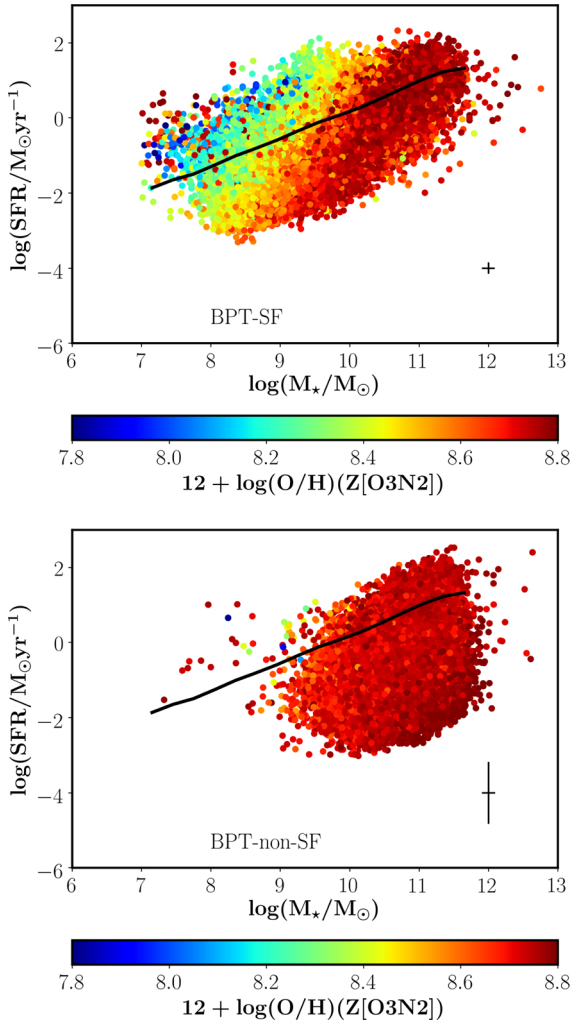


Fig. 2. SFR versus M_* for the BPT-SF (*upper-panel*) and BPT-non-SF (*lower-panel*) samples identified on the basis of [N II]-BPT. The data points are colour coded with respect to the gas-phase metallicity ($12 + \log(\text{O}/\text{H})$) using the O3N2 diagnostic described in Sect. 2.2. On both panels, the black MS line is derived from fitting a median to the SF galaxies. The error bars in the bottom-right corner indicate the median uncertainties on SFR and M_* within each subsample and are estimated from the percentiles provided in the MPA-JHU catalogue. The uncertainty on gas-phase metallicity is of the order of 0.09 dex.

spatial region (3 arcsec SDSS fibre) and the related metallicity enrichment or dilution.

Figure 2 shows, unsurprisingly, that the BPT-non-SF galaxies have SFRs typically below the SF MS – even by up to 3 dex lower –, and so they are indeed suitable for our goal of extending the FMR to galaxies approaching quiescence.

About 10% of BPT-non-SF galaxies have SFRs above the MS. This is in agreement with the results of Leslie et al. (2016), who find that there are galaxies classified as ‘composite’ or ‘ambiguous’ in the SDSS sample that lie on or above the star-forming MS. These results are also in line with those of Oemler et al. (2017), who report a large population of quiescent galaxies with disproportionately high SFRs. The fact that these highly star-forming galaxies are not classified as SF in the BPT-diagram may be a consequence of heavy obscuration (which leaves only the outer, LI(N)ER like regions visible), the presence of shocks, or nitrogen enrichment, which highlights how the simple BPT classification may be inadequate and that it can

result in a seriously biased sample. However, we find that only $\sim 2\%$ of BPT-non-SF galaxies are massive ($(\log(M_*/M_\odot) > 11)$) and have SFRs above the MS, thus ensuring that FMR results presented here are not biased by this galaxy population.

3. Results: extending the FMR to BPT-non-SF galaxies

3.1. Conventional FMR

Figure 3 shows the two projections of the conventional form of the FMR, that is, the relation between stellar mass, gas-phase metallicity, and star-formation rate. We estimated the median gas-phase metallicities in the bins of stellar mass and SFR of 0.3 dex and we retain only those which have at least 30 galaxies in each bin. The left-hand panels (Fig. 3) show the mass versus metallicity colour coded with respect to the SFR, while the right-hand panels (Fig. 3) show the SFR versus metallicity colour coded with respect to stellar mass, for the three samples as described below.

- *BPT-SF Galaxies* (Fig. 3, upper panel): The left-hand panel shows that at low stellar masses, the SF galaxies with higher SFR have lower metallicity, while at high stellar masses, there appears to be a small inversion (~ 0.05 dex) in this trend, i.e. metallicity increases with SFR. The same systematic dependence of metallicity on SFR for different stellar mass is shown in the other projection of the FMR (right-hand panel), where gas-phase metallicity is plotted with respect to SFR and each curve is colour coded with respect to the $\log M_*$.

The inversion at the high-mass end, though quite small, aligns with previous studies (e.g., Yates et al. 2012; Lara-López et al. 2013), but is in contrast to the results of Mannucci et al. (2010), the first FMR study of SF galaxies which instead shows a flattening of the gas-phase metallicity at high stellar mass. Such a difference is explained by a combined effect of different S/N cuts and different methods to estimate SFR and metallicity (Cresci et al. 2019). We reproduce the results of Mannucci et al. (2010) if we perform an S/N cut of 25 on the $\text{H}\alpha$ emission line as done in their work. Such a high S/N cut on the $\text{H}\alpha$ emission line is needed to avoid introducing metallicity biases in the lower metallicity regime, where [N II] is significantly fainter than $\text{H}\alpha$, but this S/N cut only includes SF galaxies with very high SFR, which defies the purpose of this work, which focuses on extension of the FMR to BPT-non-SF galaxies and must also include galaxies with very low SFR. Our relaxed requirement on the S/N of $\text{H}\alpha$ and $\text{H}\beta$ enables us to explore lower levels of SFR; more specifically, the minimum SFR bin in our work corresponds to $\log(\text{SFR}/M_\odot \text{yr}^{-1}) \sim -3.2$ which is significantly lower than -1.45 of Mannucci et al. (2010). The S/N cut on the [NII] line may potentially introduce a bias in the metallicity distribution; however, as we discuss below, this would make our findings even more significant. In any case, as the main purpose of this work is to extend the FMR to the LI(N)ER region (following section) where the [NII] emission is as strong as $\text{H}\alpha$, we do not expect the S/N cut on [NII] to introduce a significant bias.

- *BPT-non-SF Galaxies* (Fig. 3, middle panel): The left-hand panel shows that the gas-phase metallicity for BPT-non-SF galaxies increases with decreasing SFR for a given stellar mass lying in the range of $\log(M_*/M_\odot) \sim 10\text{--}11.5$. Similarly, the right-hand panel shows that the gas-phase metallicity of BPT-non-SF galaxies appears to be constant at high

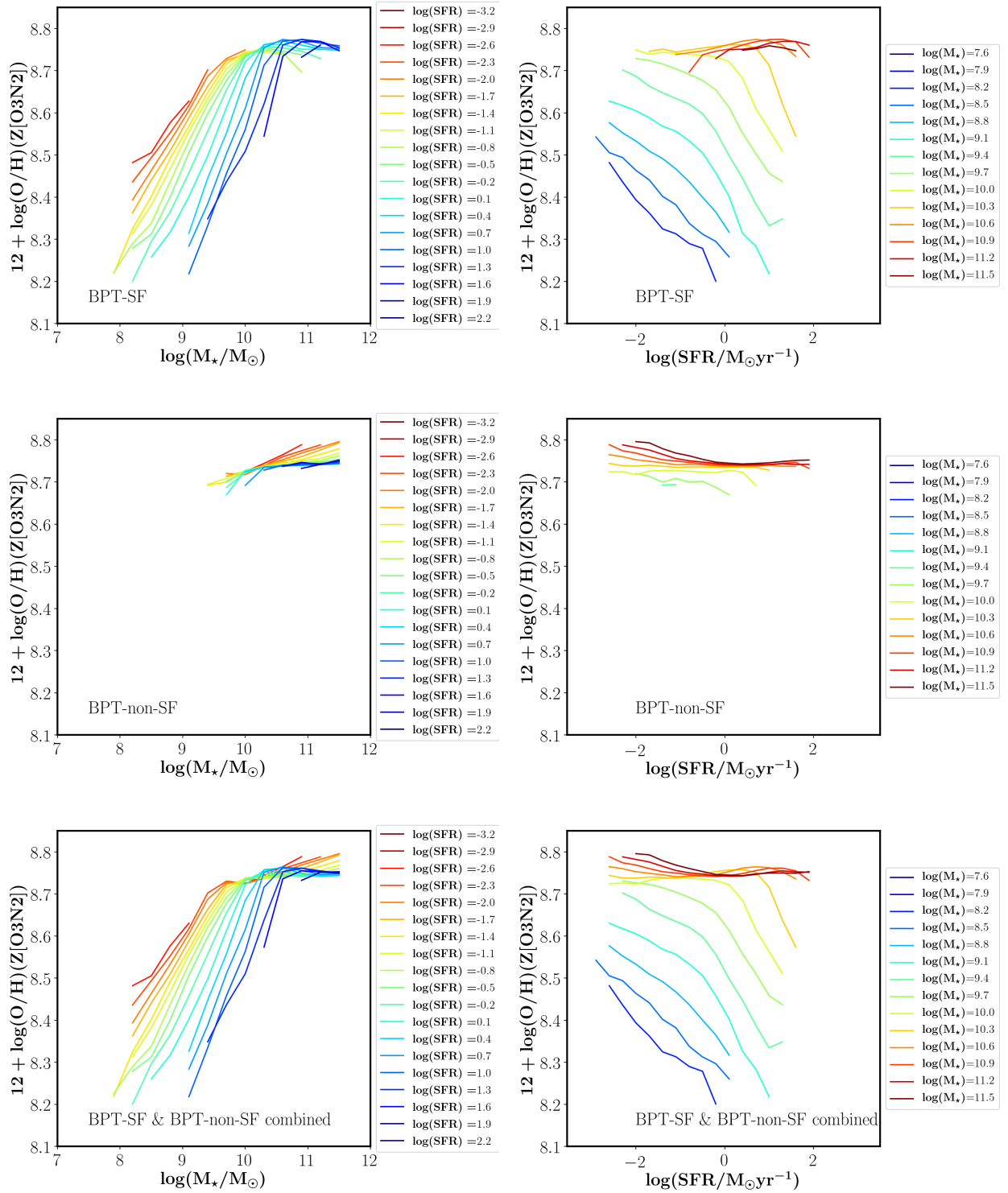


Fig. 3. *Left-hand panel:* gas-phase metallicity ($12 + \log(\text{O}/\text{H})$) versus stellar mass ($\log M_*/M_\odot$) for BPT-SF galaxies (*upper-panel*), BPT-non-SF galaxies (*middle panel*), and their combined sample (*bottom panel*). The coloured curves on each plot in the left-hand panel correspond to median metallicities estimated in the bins of $\log M_*/M_\odot$ and $\log \text{SFR}$, colour coded with respect to $\log \text{SFR}$ in a given bin. *Right-hand panel:* gas-phase metallicity ($12 + \log(\text{O}/\text{H})$) versus $\log \text{SFR}$ for BPT-SF (*upper-panel*), BPT-non-SF (*middle panel*), and their combined sample (*bottom panel*). The coloured curves on each plot in the right-hand panel correspond to the median metallicities estimated in bins of $\log \text{SFR}$ and $\log M_*/M_\odot$. The [N II]-BPT classification along with the maximum star-burst line from Kauffmann et al. (2003a) is used to separate SF (*upper-panel*) and non-SF galaxies (*middle panel*). The gas-phase metallicities of BPT-SF (*upper-panel*) and BPT-non-SF (*middle panel*) galaxies are obtained using the empirical calibrations involving the O3N2 diagnostic provided in Curti et al. (2017) and Kumari et al. (2019), respectively. The bottom panel consists of both BPT-SF and BPT-non-SF galaxies and hence their metallicities are obtained from both SF (Curti et al. 2017) and non-SF (Kumari et al. 2019) calibrations, depending on the type of galaxy populations.

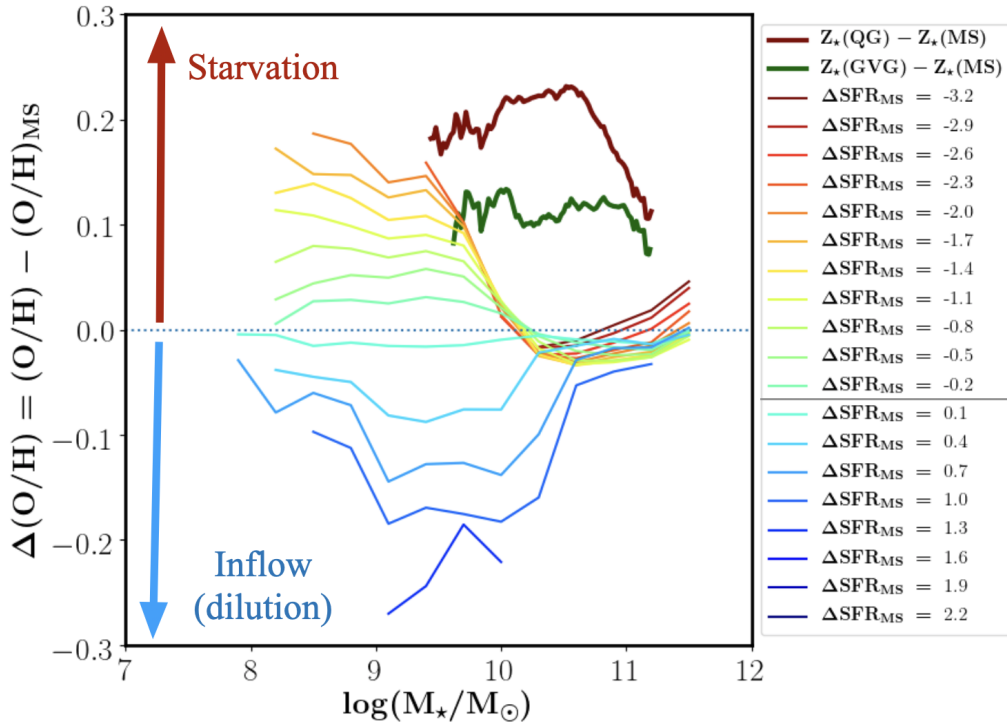


Fig. 4. Comparison of metallicity difference versus stellar mass for the gas-phase metallicity as well as for stellar metallicity for the SDSS galaxies. The gas-phase metallicity difference $\Delta(\text{O}/\text{H})$ with respect to that of MS galaxies is estimated for the combined sample of BPT-SF and BPT-non-SF galaxies identified using the $[\text{N II}]\text{-BPT}$ and is shown by thinner coloured curves corresponding to $\Delta\text{SFR}_{\text{MS}}$ varying from -3.2 to 2.2 . The thick maroon curve corresponds to the stellar metallicity difference between quiescent galaxies and MS galaxies ($Z_*(\text{QG}) - Z_*(\text{MS})$), while the thick dark green curve corresponds to the stellar metallicity difference between green valley galaxies and MS galaxies ($Z_*(\text{GVG}) - Z_*(\text{MS})$). The stellar metallicity differences are taken from [Trussler et al. \(2020\)](#).

$\log \text{SFR}/M_{\odot}\text{yr}^{-1} (> 1.0)$ for a mass range spanning an order magnitude, though we find that the gas-phase metallicity increases with increasing stellar mass for lower SFRs and that the anticorrelation of metallicity with SFR is observed primarily at $\log \text{SFR}/M_{\odot}\text{yr}^{-1} (< 1.0)$.

The high SFRs probed by this subsample is slightly counter-intuitive for galaxies classified as non-SF. However, as already mentioned, this is consistent with other works, such as [Oemler et al. \(2017\)](#), who report a large population of quiescent galaxies with disproportionately high SFRs. Such high SFRs for a non-SF classified sample comprising LINERs and AGNs are also consistent with the result of [Leslie et al. \(2016\)](#). Nevertheless, this classification has allowed us to probe, as already discussed, the massive BPT-non-SF galaxies whose SFRs are ~ 1.5 dex below the minimum SFR values probed by galaxies classified as SF (see Fig. 2), and (as already discussed) 3 dex below the MS, and thus enables us to probe a relatively quiescent population.

- *Combined sample of BPT-SF and BPT-non-SF galaxies* (Fig. 3, bottom panel): The left-hand panel shows that the mass–metallicity relation for the combined sample of BPT-SF and BPT-non-SF galaxies at the high-mass end is dominated by the BPT-non-SF galaxies which results in the disappearance of the inversion of curves seen for BPT-SF galaxies, suggesting that the latter was primarily a result of biases introduced by the BPT selection. Instead, we find that in the global (unbiased) sample, at high masses the metallicity tends to flatten with stellar mass for high SFR, but then starts to increase with decreasing SFR at $\log \text{SFR}/M_{\odot}\text{yr}^{-1} (< 0.0)$. These trends are also visible in the right-hand panel

showing metallicity versus SFR where curves are colour coded with respect to stellar mass.

3.2. Alternative representation of the FMR

Figure 4 shows an alternative representation of the FMR, where the absolute metallicity is replaced by the metallicity difference ($\Delta(\text{O}/\text{H})$) with respect to the metallicity of galaxies with the same stellar mass but located on the MS. More specifically, in Fig. 4, $\Delta(\text{O}/\text{H})$ is plotted against total stellar mass and the different curves on these plots are colour coded according to the $\Delta\text{SFR}_{\text{MS}}$, where we define $\Delta\text{SFR}_{\text{MS}} = \log(\text{SFR}) - \log(\text{SFR})_{\text{MS}}$, which is the SFR difference with respect to the SFR of galaxies on the MS at a given stellar mass. The redder curves correspond to the galaxy populations with SFRs below the MS, while the bluer curves correspond to those galaxy populations whose SFR is above the MS.

We find that the gas-phase metallicity of galaxy populations with an SFR higher than that of MS galaxies is metal-poor compared to the metallicity of these latter, and that this deficiency becomes more prominent the further galaxies deviate from the MS, although the effect is less prominent at high stellar masses. Conversely, the gas-phase metallicity of galaxies with an SFR lower than that of MS galaxies is more metal-rich, but this effect is primarily seen at low stellar masses; the metallicity excess increases with deviation from the MS, but steeply decreases with increasing stellar mass, becoming consistent with MS galaxies before the difference increases again at high stellar masses for galaxies with an SFR well below that of MS galaxies.

We also note that we are looking at the relative trends here where the relative uncertainty (due to binning) is much smaller than the absolute uncertainty on metallicity calibration, SFR, and M_* . Therefore, relative variations, although small, are quite significant.

4. Discussion and conclusions

On the MS, galaxies are commonly believed to be in a quasi-steady equilibrium between inflows, outflows, and star formation. An increase in star formation relative to the MS must be associated with either an increase in the additional gas from extra inflow or an increased star formation efficiency. A decrease in star formation relative to the MS must be associated with a shortage of gas due to either removal by extra outflows or processes (e.g., halo heating, [Birnbom et al. 2007](#); [van de Voort et al. 2011](#); [Churchill et al. 2012](#); [Johansson et al. 2012](#)) preventing gas accretion, resulting in ‘starvation’, or a decrease in star formation efficiency.

Recent works investigating the gas content in galaxies have revealed that deviations from the MS result from variations in gas content and star formation efficiency ([Schreiber et al. 2016](#); [Saintonge et al. 2017](#); [Tacconi et al. 2018](#); [Piotrowska et al. 2020](#); [Zhang et al. 2019](#); [Dou et al. 2021](#)). The metallicity of galaxies provides an additional tool with which to investigate these aspects. For instance, as discussed in [Mannucci et al. \(2010\)](#) and [Bothwell et al. \(2013, 2016b\)](#), the lower metallicity observed for highly star forming galaxies is likely associated with an increase in gas inflow that both boosts star formation and dilutes the gas-phase metallicity (an alternative explanation is that the increased star formation drives more powerful metal-loaded outflows, but the stronger anti-correlation with gas content favours the inflow-dilution scenario). As already mentioned in Sect. 1, [Peng et al. \(2015\)](#) and [Trussler et al. \(2020\)](#) show that the average stellar metallicity of passive and green-valley galaxies is higher than MS galaxies (especially for what concerns high redshift progenitors of passive galaxies) and that this can only be explained in terms of quenching being primarily associated with ‘starvation’, that is, suppression of gas inflow that on the one hand results in suppression of star formation (as the residual gas is being consumed by star formation) while on the other causes an increase in the metallicity as the dilution effect of inflow is reduced.

We now have the opportunity to investigate the same effects using the gas metallicity for galaxies spanning a broad range of offsets from the MS, including galaxies not classified as star forming in the BPT diagrams, which enables us to delve better into the green valley and quiescent region, where galaxies typically have LINER-like emission lines (which were generally excluded by previous studies of the FMR).

We can now interpret the metallicity trends shown in Fig. 4 relative to MS galaxies in the context of the scenarios discussed above. Those galaxies with positive $\Delta\text{SFR}_{\text{MS}}$, that is, above that of the MS galaxies, have metallicities lower than their counterparts on the MS, i.e. $\Delta(\text{O}/\text{H})$ is always < 0 . As mentioned above, this effect can be interpreted in terms of gas inflows dominating the galaxies lying above the MS, which both dilute the gas-phase metallicity and boost star formation.

The behaviour of galaxies below the MS (negative $\Delta\text{SFR}_{\text{MS}}$) is more complex. At low masses, the gas metallicity is clearly higher than in MS galaxies, therefore favouring a chemical evolution of these systems in which the metallicity increases as a consequence of lack of dilution from the inflow of fresh gas, i.e. the starvation scenario. In these galaxies, the chemical

enrichment tends to proceed more in a closed-box or leaky-box scenario, in which galaxies are out of equilibrium and the metallicity increases more steeply than for the MS galaxies in which star formation and outflows are balanced by inflows. Qualitatively, this is the same result as that obtained by [Peng et al. \(2015\)](#) and [Trussler et al. \(2020\)](#) for the stellar metallicities. However, quantitatively the result is quite different. The stellar metallicity difference between passive and MS galaxies (and between green valley and MS galaxies), as inferred from [Trussler et al. \(2020\)](#), is illustrated in Fig. 4 with a thick red line (and with a thick green line for green valley galaxies). At low stellar masses, the gas metallicity differences are similar to the stellar metallicity difference, supporting the same starvation scenario. However, at high and intermediate stellar masses ($\geq 10^{10} M_{\odot}$), although there is still some visible effect of the gas metallicity difference increasing with the deviation from the MS, quantitatively the gas metallicity differences are much smaller than the stellar metallicity differences. This is clearly indicating that the stellar population of massive galaxies below the MS has not formed out of gas with the same chemical properties as the gas that we are currently observing in these systems.

A possible scenario is that, in the case of the massive galaxies below the MS for which we can measure the gas-phase metallicity, we are observing them in a peculiar evolutionary stage. Indeed, in order to measure the metallicity, we need to detect nebular emission lines that, for passive and green-valley galaxies, are typically characterised by LI(N)ER-like ratios, especially in the central region probed by the SDSS fibre ([Belfiore et al. 2017](#)). However, the majority of passive galaxies are line-less, and so for the majority of quiescent galaxies we cannot effectively measure the gas metallicity. Therefore, a likely scenario is that the small fraction of quiescent galaxies that have nebular emission (and for which we can measure the gas metallicity) may have an excess of gas because they have recently accreted gas from the circumgalactic and/or intergalactic medium (hence typically with metallicity lower than the stellar metallicity of the accreting massive galaxy) and therefore in this case the observed gas is anomalously metal poor relative to their quiescent parent population. In a few cases, this gas accretion may result in a rejuvenation event, with the accreted gas forming stars, as indeed observed in some massive galaxies ([Chaume et al. 2019](#)). However, as already emphasised, in most cases the accreted gas has LIER-like emission, i.e. not associated with star formation; it is likely ionised by the hard radiation field of the evolved (post-AGB) stars. Such hard radiation field is likely responsible for keeping the accreted gas hot and ionised and preventing it from forming stars. Such accreted gas may also likely be expelled at later times by the SNIa cumulative energy (see [Trussler et al. 2020](#); [Pipino & Matteucci 2004](#); [Matteucci et al. 2006](#)) and also by the energy injected by a weak AGN ([Ciotti & Ostriker 2007](#); [Ciotti et al. 2009](#)). This effect of gas accretion with little SF associated with it may also be responsible for the offset between stellar and gas metallicity for galaxies below the MS at low and intermediate masses. We also find that $\sim 78\%$ of galaxies lying in the mass range $8 < \log(M_*/M_{\odot}) < 9$ have $\Delta(\text{O}/\text{H}) > 0$, implying that the majority of dwarf galaxies are going through a starvation phase rather than dilution via gas accretion.

In summary, our results support the scenario in which, for galaxies above the MS, the lower metallicity is associated with the dilution effect of gas accretion. For galaxies below the MS, at low masses their higher metallicity is in accordance with the scenario in which their quenching involves starvation (suppression of gas inflows); outflows may also play a role in quenching,

but starvation is necessary to account for the increased gas-phase metallicity relative to MS galaxies. At high masses, the fact that galaxies below the MS have gas-phase metallicities closer to those of the MS galaxies while their stellar metallicities are much higher than galaxies on the MS suggests that we are observing these galaxies in a peculiar phase, in which they have recently accreted gas, but this accreted gas is prevented from forming stars (in agreement with the independent findings that the efficiency of star formation decreases drastically toward the quiescent region).

This study has allowed us to extend the FMR to the BPT-non-SF galaxies in the local Universe, and is a step forward in piecing together different evolutionary stages of BPT-non-SF galaxies dominated by different physical processes. Recent surveys have pointed out the presence of a substantial population of non-SF quiescent galaxies in the high-redshift Universe, though spectroscopy information on these populations is still sparse (McCracken et al. 2012; Straatman et al. 2016; Muzzin et al. 2013; Schreiber et al. 2018; Morishita et al. 2019; Whitaker et al. 2013; Glazebrook et al. 2017; Santini et al. 2019; Merlin et al. 2018). The upcoming Multi-Object Optical and Near-infrared Spectrograph (MOONS; Cirasuolo et al. 2020) at the VLT will enable extensive spectroscopic follow-up of such imaging surveys (Maiolino et al. 2020), hence enabling us to explore the FMR for BPT-non-SF galaxies in the distant Universe, and understand the physical processes driving quenching and chemical enrichment at different epochs in the history of the Universe.

Acknowledgements. N. K. acknowledges the fellowship from the Schlumberger Foundation which supported her stay at KICC where most of the work was accomplished. M. C., R. M. and J. T. acknowledge ERC Advanced Grant 695671 “QUENCH” and support by the Science and Technology Facilities Council (STFC). This research made use of the on SDSS archival data, that can be retrieved from <https://www.mpa.mpa-garching.mpg.de/SDSS/DR7/> and Astropy, a community-developed core Python package for Astronomy (Astropy Collaboration 2013).

References

- Abazajian, K. N., Adelman-McCarthy, J. K., Agüeros, M. A., et al. 2009, *ApJS*, **182**, 543
- Andrews, B. H., & Martini, P. 2013, *ApJ*, **765**, 140
- Astropy Collaboration (Robitaille, T. P., et al.) 2013, *A&A*, **558**, A33
- Baldwin, J. A., Phillips, M. M., & Terlevich, R. 1981, *PASP*, **93**, 5
- Barrera-Ballesteros, J. K., Sánchez, S. F., Heckman, T., Blanc, G. A., & MaNGA Team 2017, *ApJ*, **844**, 80
- Belfiore, F., Maiolino, R., Maraston, C., et al. 2016, *MNRAS*, **461**, 3111
- Belfiore, F., Maiolino, R., Maraston, C., et al. 2017, *MNRAS*, **466**, 2570
- Belfiore, F., Maiolino, R., Bundy, K., et al. 2018, *MNRAS*, **477**, 3014
- Birnboim, Y., Dekel, A., & Neistein, E. 2007, *MNRAS*, **380**, 339
- Bothwell, M. S., Maiolino, R., Kennicutt, R., et al. 2013, *MNRAS*, **433**, 1425
- Bothwell, M. S., Maiolino, R., Ciccone, C., Peng, Y., & Wagg, J. 2016a, *A&A*, **595**, A48
- Bothwell, M. S., Maiolino, R., Peng, Y., et al. 2016b, *MNRAS*, **455**, 1156
- Bourne, N., Dunne, L., Maddox, S. J., et al. 2016, *MNRAS*, **462**, 1714
- Brinchmann, J., Charlot, S., White, S. D. M., et al. 2004, *MNRAS*, **351**, 1151
- Brisbin, D., & Harwit, M. 2012, *ApJ*, **750**, 142
- Brown, T., Cortese, L., Catinella, B., & Kilborn, V. 2018, *MNRAS*, **473**, 1868
- Bryant, J. J., Owers, M. S., Robotham, A. S. G., et al. 2015, *MNRAS*, **447**, 2857
- Bundy, K., Bershady, M. A., Law, D. R., et al. 2015, *ApJ*, **798**, 7
- Bustamante, S., Sparre, M., Springel, V., & Grand, R. J. J. 2018, *MNRAS*, **479**, 3381
- Charlot, S., & Longhetti, M. 2001, *MNRAS*, **323**, 887
- Chaue, P., van der Wel, A., Pacifci, C., et al. 2019, *ApJ*, **877**, 48
- Churchill, C. W., Kacprzak, G. G., Steidel, C. C., et al. 2012, *ApJ*, **760**, 68
- Ciotti, L., & Ostriker, J. P. 2007, *ApJ*, **665**, 1038
- Ciotti, L., Ostriker, J. P., & Proga, D. 2009, *ApJ*, **699**, 89
- Cirasuolo, M., Fairley, A., Rees, P., et al. 2020, *Messenger*, **180**, 10
- Cresci, G., Mannucci, F., Sommariva, V., et al. 2012, *MNRAS*, **421**, 262
- Cresci, G., Mannucci, F., & Curti, M. 2019, *A&A*, **627**, A42
- Curti, M., Cresci, G., Mannucci, F., et al. 2017, *MNRAS*, **465**, 1384
- Curti, M., Mannucci, F., Cresci, G., & Maiolino, R. 2020, *MNRAS*, **491**, 944
- Davé, R., Finlator, K., & Oppenheimer, B. D. 2011, *MNRAS*, **416**, 1354
- Dayal, P., Ferrara, A., & Dunlop, J. S. 2013, *MNRAS*, **430**, 2891
- De Rossi, M. E., Theuns, T., Font, A. S., & McCarthy, I. G. 2015, *MNRAS*, **452**, 486
- De Rossi, M. E., Bower, R. G., Font, A. S., Schaye, J., & Theuns, T. 2017, *MNRAS*, **472**, 3354
- Dou, J., Peng, Y., Renzini, A., et al. 2021, *ApJ*, **907**, 114
- Ellison, S. L., Patton, D. R., Simard, L., & McConnachie, A. W. 2008, *ApJ*, **672**, L107
- Forbes, J. C., Krumholz, M. R., Burkert, A., & Dekel, A. 2014, *MNRAS*, **443**, 168
- Gallazzi, A., Charlot, S., Brinchmann, J., White, S. D. M., & Tremonti, C. A. 2005, *MNRAS*, **362**, 41
- Gallazzi, A., Bell, E. F., Zibetti, S., Brinchmann, J., & Kelson, D. D. 2014, *ApJ*, **788**, 72
- Genel, S. 2016, *ApJ*, **822**, 107
- Glazebrook, K., Schreiber, C., Labbé, I., et al. 2017, *Nature*, **544**, 71
- Gobat, R., Daddi, E., Magdis, G., et al. 2018, *Nat. Astron.*, **2**, 239
- Heckman, T. M. 1980, *A&A*, **500**, 187
- Hunt, L., Dayal, P., Magrini, L., & Ferrara, A. 2016, *MNRAS*, **463**, 2002
- Johansson, P. H., Naab, T., & Ostriker, J. P. 2012, *ApJ*, **754**, 115
- Kashino, D., Renzini, A., Silverman, J. D., & Daddi, E. 2016, *ApJ*, **823**, L24
- Kauffmann, G., Heckman, T. M., Tremonti, C., et al. 2003a, *MNRAS*, **346**, 1055
- Kauffmann, G., Heckman, T. M., White, S. D. M., et al. 2003b, *MNRAS*, **341**, 33
- Kennicutt, R. C., Jr 1998, *ApJ*, **498**, 541
- Kewley, L. J., Groves, B., Kauffmann, G., & Heckman, T. 2006, *MNRAS*, **372**, 961
- Kroupa, P. 2001, *MNRAS*, **322**, 231
- Kumari, N., Maiolino, R., Belfiore, F., & Curti, M. 2019, *MNRAS*, **485**, 367
- Lagos, C. d. P., Theuns, T., Schaye, J., et al. 2016, *MNRAS*, **459**, 2632
- Lara-López, M. A., López-Sánchez, Á. R., & Hopkins, A. M. 2013, *ApJ*, **764**, 178
- Lequeux, J., Peimbert, M., Rayo, J. F., Serrano, A., & Torres-Peimbert, S. 1979, *A&A*, **80**, 155
- Leslie, S. K., Kewley, L. J., Sanders, D. B., & Lee, N. 2016, *MNRAS*, **455**, L82
- Lian, J. H., Li, J. R., Yan, W., & Kong, X. 2015, *MNRAS*, **446**, 1449
- Lilly, S. J., Carollo, C. M., Pipino, A., Renzini, A., & Peng, Y. 2013, *ApJ*, **772**, 119
- Maiolino, R., & Mannucci, F. 2019, *A & Arv*, **27**, 3
- Maiolino, R., Nagao, T., Grazian, A., et al. 2008, *A&A*, **488**, 463
- Maiolino, R., Cirasuolo, M., Afonso, J., et al. 2020, *Messenger*, **180**, 24
- Mannucci, F., Cresci, G., Maiolino, R., Marconi, A., & Gnerucci, A. 2010, *MNRAS*, **408**, 2115
- Mannucci, F., Salvaterra, R., & Campisi, M. A. 2011, *MNRAS*, **414**, 1263
- Maraston, C., & Strömbäck, G. 2011, *MNRAS*, **418**, 2785
- Matteucci, F., Panagia, N., Pipino, A., et al. 2006, *MNRAS*, **372**, 265
- Matthee, J., & Schaye, J. 2018, *MNRAS*, **479**, L34
- McCracken, H. J., Milvang-Jensen, B., Dunlop, J., et al. 2012, *A&A*, **544**, A156
- Merlin, E., Fontana, A., Castellano, M., et al. 2018, *MNRAS*, **473**, 2098
- Morishita, T., Abramson, L. E., Treu, T., et al. 2019, *ApJ*, **877**, 141
- Muzzin, A., Marchesini, D., Stefanon, M., et al. 2013, *ApJ*, **777**, 18
- Nakajima, K., & Ouchi, M. 2014, *MNRAS*, **442**, 900
- Oemler, A. J., Abramson, L. E., Gladders, M. D., et al. 2017, *ApJ*, **844**, 45
- Peng, Y., Maiolino, R., & Cochrane, R. 2015, *Nature*, **521**, 192
- Piotrowska, J. M., Bluck, A. F. L., Maiolino, R., Concas, A., & Peng, Y. 2020, *MNRAS*, **492**, L6
- Pipino, A., & Matteucci, F. 2004, *MNRAS*, **347**, 968
- Popesso, P., Concas, A., Morselli, L., et al. 2019, *MNRAS*, **483**, 3213
- Renzini, A., & Peng, Y.-J. 2015, *ApJ*, **801**, L29
- Romeo Velonà, A. D., Sommer-Larsen, J., Napolitano, N. R., et al. 2013, *ApJ*, **770**, 155
- Roseboom, I. G., Bunker, A., Sumiyoshi, M., et al. 2012, *MNRAS*, **426**, 1782
- Saintonge, A., Catinella, B., Tacconi, L. J., et al. 2017, *ApJS*, **233**, 22
- Salim, S., Rich, R. M., Charlot, S., et al. 2007, *ApJS*, **173**, 267
- Salim, S., Lee, J. C., Ly, C., et al. 2014, *ApJ*, **797**, 126
- Salim, S., Lee, J. C., Janowiecki, S., et al. 2016, *ApJS*, **227**, 2
- Sánchez, S. F., Kennicutt, R. C., Gil de Paz, A., et al. 2012, *A&A*, **538**, A8
- Sánchez, S. F., Barrera-Ballesteros, J. K., López-Cobá, C., et al. 2019, *MNRAS*, **484**, 3042
- Sánchez Almeida, J., & Sánchez-Menguiano, L. 2019, *ApJ*, **878**, L6
- Sánchez-Blázquez, P., Peletier, R. F., Jiménez-Vicente, J., et al. 2006, *MNRAS*, **371**, 703
- Sanders, R. L., Shapley, A. E., Kriek, M., et al. 2018, *ApJ*, **858**, 99
- Sanders, R. L., Shapley, A. E., Reddy, N. A., et al. 2020, *MNRAS*, **491**, 1427

- Santini, P., Merlin, E., Fontana, A., et al. 2019, *MNRAS*, 486, 560
- Schmidt, M. 1959, *ApJ*, 129, 243
- Schreiber, C., Elbaz, D., Pannella, M., et al. 2016, *A&A*, 589, A35
- Schreiber, C., Glazebrook, K., Nanayakkara, T., et al. 2018, *A&A*, 618, A85
- Singh, R., van de Ven, G., Jahnke, K., et al. 2013, *A&A*, 558, A43
- Spitoni, E., Vincenzo, F., & Matteucci, F. 2017, *A&A*, 599, A6
- Stasińska, G., Vale Asari, N., Cid Fernandes, R., et al. 2008, *MNRAS*, 391, L29
- Straatman, C. M. S., Spitler, L. R., Quadri, R. F., et al. 2016, *ApJ*, 830, 51
- Tacconi, L. J., Genzel, R., Saintonge, A., et al. 2018, *ApJ*, 853, 179
- Telford, O. G., Dalcanton, J. J., Skillman, E. D., & Conroy, C. 2016, *ApJ*, 827, 35
- Torrey, P., Vogelsberger, M., Hernquist, L., et al. 2018, *MNRAS*, 477, L16
- Tremonti, C. A., Heckman, T. M., Kauffmann, G., et al. 2004, *ApJ*, 613, 898
- Troncoso, P., Maiolino, R., Sommariva, V., et al. 2014, *A&A*, 563, A58
- Trussler, J., Maiolino, R., Maraston, C., et al. 2020, *MNRAS*, 491, 5406
- Trussler, J., Maiolino, R., Maraston, C., et al. 2021, *MNRAS*, 500, 4469
- van de Voort, F., Schaye, J., Booth, C. M., Haas, M. R., & Dalla Vecchia, C. 2011, *MNRAS*, 414, 2458
- Whitaker, K. E., van Dokkum, P. G., Brammer, G., et al. 2013, *ApJ*, 770, L39
- Wilkinson, D. M., Maraston, C., Goddard, D., Thomas, D., & Parikh, T. 2017, *MNRAS*, 472, 4297
- Yates, R. M., Kauffmann, G., & Guo, Q. 2012, *MNRAS*, 422, 215
- York, D. G., Adelman, J., Anderson, J. E. Jr., et al. 2000, *AJ*, 120, 1579
- Zhang, C., Peng, Y., Ho, L. C., et al. 2019, *ApJ*, 884, L52

Appendix A: Alternative FMR using [S II]-BPT with and without AGNs

Figure A.1 shows the alternative representation of the FMR where star-forming and non star-forming samples have been identified using the [S II]-BPT classification. The metallicities of the BPT-SF sample have been determined using the O3N2 calibration from Curti et al. (2017) while for the BPT-non-SF sample, we applied the correction to these metallicities given by Kumari et al. (2019) for [S II]-BPT classification. The sample in the upper panel includes AGNs while that in the lower panel excludes them. The overall behaviour of the FMR for both samples (with and without AGNs) selected on the basis of [S II]-BPT is similar to that found in Fig. 4 where [N II]-BPT was used for sample selection. This shows that the FMR behaviour is independent of the inclusion or removal of AGNs. This strengthens our results from [N II]-BPT classification where AGNs could not be excluded for lack of a recipe. We find however that metallicity differences for the massive galaxies in the [S II]-BPT selected sample hardly go beyond zero (Fig. A.1), in contrast to the [N II]-BPT selected sample (Fig. 4). This is likely because the initial O3N2 calibration from (Curti et al. 2017) is devised from the [N II]-BPT-selected sample and not the [S II]-BPT-selected sample.

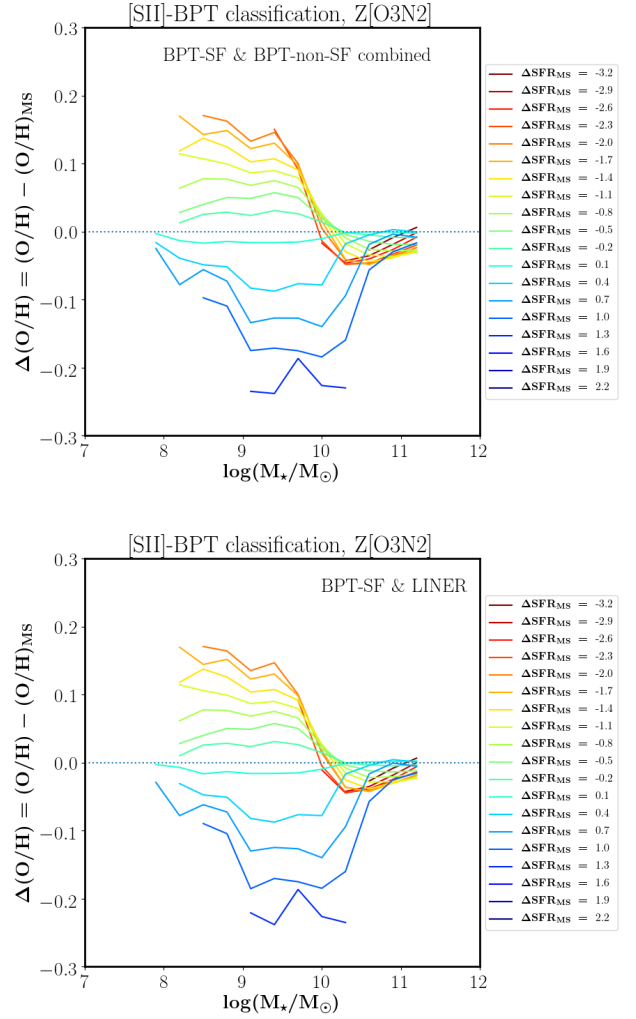


Fig. A.1. $\Delta(\text{O}/\text{H})$ versus stellar mass ($\log M_*/M_\odot$) for the entire sample comprised of BPT-SF and BPT-non-SF galaxies where [S II]-BPT is used for galaxy classification. The sample in the upper-panel includes AGNs while the sample in the lower panel excludes AGNs. The coloured curves in each plot correspond to median $\Delta(\text{O}/\text{H})$ estimated in bins of $\log M_*/M_\odot$ and $\Delta\text{SFR}_{\text{MS}}$ and colour-coded with respect to $\Delta\text{SFR}_{\text{MS}}$ in a given bin.